Journal of Materials Chemistry A

PAPER

View Article Online
View Journal | View Issue

Cite this: *J. Mater. Chem. A*, 2017, **5**, 7026

Novel hybrid Si nanocrystals embedded in a conductive SiO_x@C matrix from one single precursor as a high performance anode material for lithium-ion batteries†

Min Zhu, Jie Yang, Zhihao Yu, Haibiao Chen* and Feng Pan*

Received 10th February 2017
Accepted 13th March 2017

DOI: 10.1039/c7ta01254c

rsc.li/materials-a

Silicon (Si) is a promising anode material for lithium-ion batteries (LIBs) owing to its very high lithium storage capacity; however, fragmentation of Si caused by drastic volume change during lithium insertion and extraction leads to serious capacity decay during cycling. In this work, we report a novel method to synthesize an *in situ* nanocomposite containing Si nanoparticles evenly embedded in an electrically conductive SiO_x@C network (Si/SiO_x@C) from one single polysiloxane precursor. In our process, Si nanocrystals were reduced from the polysiloxane precursor using a low temperature molten salt reduction method, and carbon segregated out in the SiO_x@C phase which evolved during the subsequent pyrolysis. As an anode material for LIBs, the Si/SiO_x@C nanocomposite showed a specific capacity up to 1292 mA h g^{-1} at a current density of 0.4 A g^{-1} and 81.84% capacity retention after 200 cycles. The high capacity and stable performance of Si/SiO_x@C as an anode material can be attributed to the continuous SiO_x@C matrix which provides reliable mechanical support, electronic and ionic conductivity, and a stable solid–electrolyte interphase (SEI). This work demonstrated the viability of deriving a homogenous nanocomposite from a single polymeric precursor, which creates a promising anode material for next-generation LIBs.

Introduction

Electric vehicles (EVs) running on rechargeable batteries with very low emissions are considered as one important solution to environmental degradation and the energy crisis.[1] Extending the range per charge of EVs to be comparable to that of traditional fuel-powered vehicles is a demanding challenge, which relies on continued improvement in the capacity of lithium-ion batteries (LIBs). For LIBs, Si-based anode materials attract extensive research interest because the specific capacity of Si (3579 mA g^{-1}) is nearly 10 times higher than that of commercial graphite anodes.[2] However, the significant volume expansion of Si upon being charged and corresponding volume shrinkage upon being discharged have caused serious issues in the anode, such as pulverization of Si, delamination of the active layer, and erratic solid–electrolyte interphase (SEI) formation. Also, the low electric conductivity of Si severely affects the performance of Si-based anodes.[3,4]

In order to improve the electrochemical performance of Si-based anodes, researchers have explored various approaches. Nanostructured Si, including Si nanowires,[5–7] nanotubes,[8,9] nanoparticles,[7,10–12] and porous Si,[13–16] can accommodate the volume change caused by lithium insertion/extraction and has been widely demonstrated to effectively suppress pulverization. In addition, various Si-containing composite structures have been shown to further improve the performance of these anodes.[4,14,17–27] Wrapping Si particles in a flexible and conductive shell or matrix can improve the electronic conductivity as well as the durability of these anodes, as the shell or the matrix can prevent the loss of disintegrated Si, transfer electrons and lithium ions, and stabilize the SEI. Since the formation of a new SEI consumes lithium and causes capacity decay, a stable SEI is desirable for Si-based anodes. Cui's group demonstrated that when enclosed in conformal graphene cages, even Si microparticles (1–3 μm) could maintain a stable capacity during cycling.[28] Although these Si microparticles inevitably fractured during cycling, they were enclosed in the graphene cages at all times, which ensured that fractured Si particles could maintain constant electrical contacts and would not be in direct contact with the electrolyte. SEI films only formed around the external surface of the graphene cages and would not form around individual fractured Si particles, which helped retain the lithium storage capacity of Si. Moreover, Si-based compounds were also explored as alternative Li-storage materials besides elemental Si. Silicon oxycarbide (SiOC) can offer a specific

School of Advanced Materials, Peking University, Shenzhen Graduate School, Shenzhen 518055, People's Republic of China. E-mail: chenhb@pkusz.edu.cn; panfeng@pkusz.edu.cn

† Electronic supplementary information (ESI) available: Additional characterization data. See DOI: 10.1039/c7ta01254c

capacity of 600–800 mA h g^{-1} as an anode material, and it exhibits superior cycling stability.[29–31] SiOC materials are typically prepared by thermal conversion of polysiloxanes and can be described using a composition of $SiC_xO_{4-x} + yC_{free}$.[32] SiOC has a structure similar to SiO_x. By substituting some oxygen atoms with carbon atoms, SiOC gains better rigidity, strength, and cycling performance as an anode material.[33–38] Also, SiOC with free carbon (SiO_x@C) constitutes a continuous matrix which offers excellent electronic conductivity.[29,30] In order to take advantage of both Si and SiO_x@C, researchers have tried embedding Si in a matrix of SiO_x@C.[33,39,40] Most previous studies on Si composite anodes used a common approach by enclosing existing Si particles with carbon or other conductive matrices.

In this work, we demonstrate that an *in situ* nanocomposite consisting of Si nanoparticles embedded in a matrix of SiO_x@C can be prepared from a single precursor. Since polysiloxane, which is commonly known as "silicone", contains both silicon and carbon, it can serve as the source of both Si and C. Magnesiothermic reduction has been developed as an effective method to produce nanocrystalline-Si from many SiO_2-based precursors.[41–43] Recently, a low temperature molten salt reduction method has been developed by Lin *et al.* to produce elemental Si from SiO_2 using magnesium as a reducing agent.[12] Based on the same concept, we were able to reduce Si from a polysiloxane precursor and obtain Si nanoparticles dispersed in the remaining polymer. After subsequent pyrolysis, we obtained a nanocomposite in which Si nanoparticles were homogenously dispersed in a matrix of SiO_x@C. In this process, no existing Si nanoparticles were used and both the Si nanoparticles and the SiO_x@C matrix were synthesized *in situ*. The low temperature molten salt reduction method suppresses the formation of the electrochemically inactive SiC. The Si/SiO_x@C nanocomposite used as an anode material for LIBs showed a specific capacity up to 1292 mA h g^{-1} at a current density of 400 mA g^{-1} and a capacity retention of 81.84% after 200 cycles. In the Si/SiO_x@C nanocomposite, the Si nanoparticles contribute to lithium storage, and the free carbon within the SiO_x@C matrix serves as a conducting network for electrons and lithium ions. The volume variation of the Si nanoparticles can be accommodated by the surrounding SiO_x phase and the carbon network. Meanwhile, a stable SEI film can be maintained since Si is isolated from the electrolyte. The Si/SiO_x@C anode exhibited a superior stability in comparison to a nanocrystalline Si anode.

Experimental

The synthesis procedure of the Si/SiO_x@C nanocomposite is illustrated in Scheme 1. We first reacted vinyl-terminated poly(methylphenylsiloxane) with polymethylhydrosiloxane to produce a cross-linked polysiloxane elastomer with a translucent appearance (denoted as P1). In order to produce Si, we sealed P1, Mg and $AlCl_3$ together in a stainless steel hydrothermal reactor under nitrogen. After being heated at 245 °C for 10 h, Si in P1 was reduced to form Si nanoparticles, which were uniformly embedded in a polymer matrix and the composite had a dark brown color (designated as Si/P2). Si/P2 was further pyrolyzed at 900 °C in argon for 4 h and the polymer matrix was converted into the SiO_x@C matrix. Since Si and C are evenly distributed in P1 at the atomic level, it is expected that an overall homogenous distribution of Si and C in the final product Si/SiO_x@C can be achieved.

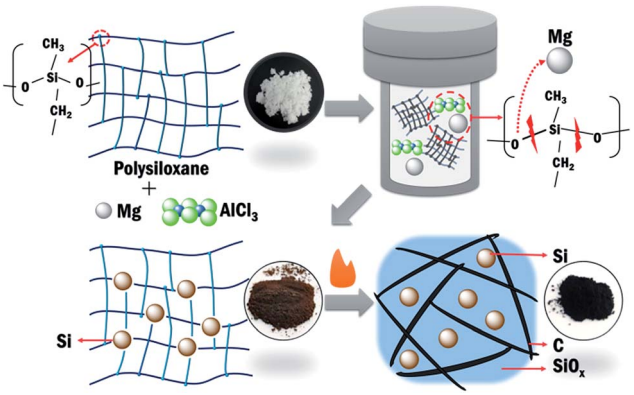

Scheme 1 Synthesis of the Si/SiO_x@C *in situ* nanocomposite from a single polysiloxane precursor.

Synthesis of the polysiloxane precursor (P1)

Polymethylhydrosiloxane (PMHS, Sigma-Aldrich) was used as a cross-linking agent to cure vinyl-terminated poly(methylphenylsiloxane) (UC252, Jiaxing United Chemical Co., China) into a silicone elastomer. In a typical procedure, 0.5 gram of PMHS, 10 grams of UC252, and 15 μL 2 wt% Pt catalyst solution (platinum(0)-1,3-divinyl-1,1,3,3-tetramethyldisiloxane complex solution in xylene, Sigma-Aldrich) were mixed in a disposable cup and manually stirred for 10 min. The mixture was left undisturbed at room temperature overnight, and then it was heated to 360 °C for 100 min in a tube furnace under an argon flow. After cooling down to room temperature, the product P1 was collected and ground into powder.

Preparation of Si/P2 and Si/SiO_x@C nanocomposites

8 g of $AlCl_3$ (Aladdin), 1 g of magnesium powder (Aladdin), and 1 g of precursor P1 were mixed and loaded in a 20 mL stainless steel hydrothermal synthesis reactor. The reactor was heated at 245 °C for 10 h in an oven. After cooling down to room temperature, the product was collected and washed with 0.2 M hydrochloric acid, distilled water, and ethanol several times to remove the metal compounds which were by-products. The resulting Si/P2 material was dried in an oven at 180 °C for 6 h. The Si/P2 material was heated under an argon atmosphere to 900 °C at a ramp rate of 5 °C min^{-1} and maintained at this temperature for 4 h. After cooling down to room temperature, the product Si/SiO_x@C was collected.

Physical characterization

The phases in the Si/P2 and Si/SiO_x@C nanocomposites were analyzed using X-ray diffraction (XRD, Bruker D8 Advance diffractometer using Cu Kα radiation, $\lambda = 1.5405$ Å). Raman

spectra were measured on an iHR320 spectrometer with a Synapse CCD detector (Horiba Instruments Inc). Scanning electron microscopy (SEM) was performed with a field emission scanning electron microscope (ZEISS Supra 55). Transmission electron microscopy (TEM) images were obtained using an FEI TecnaiG2 F30. Fourier transform infrared (FTIR) spectra of the materials were collected using a Perkin Elmer Frontier spectrometer. Thermogravimetric analysis (TGA) was performed using a Mettler-Toledo TGA/DSC-1 system. X-ray photoelectron spectra (XPS) were obtained using an ESCALAB 250XL X-ray photoelectron spectrometer.

Electrochemical measurements

The electrochemical properties of the Si/SiO_x@C composite as an anode material for LIBs were investigated using a half-cell configuration. The Si/SiO_x@C material was first mixed with super P and poly(acrylic acid) (PAA, $M_w = 3\ 000\ 000$, Aldrich) in a weight ratio of 70 (Si/SiO_x@C) : 15 (super P) : 15 (PAA), followed by drying at 80 °C for 24 h under vacuum. Lithium foil was used as the counter electrode and a Celgard® 2400 microporous membrane was used as the separator. An electrolyte containing 1 M lithium hexafluorophosphate ($LiPF_6$) solution in co-solvents of ethylene carbonate (EC) and diethyl carbonate (DEC) (1 : 1, v/v) containing 5 wt% fluoroethylenecarbonate (FEC, PANAX E-TEC, Korea) was used. The galvanostatic charging and discharging experiments were performed on a Neware battery testing system in the voltage range of 0.01–2.0 V (*vs.* Li^+/Li) at 25 °C. In the cycling performance test, all of the samples were run for 3 pre-cycles at 0.1 A g^{-1} for 3 rounds, and then were run at 0.4 A g^{-1} in the subsequent cycles.

Results and discussion

The morphology of Si/P2 and Si/SiO_x@C was first observed using SEM and the images are shown in Fig. 1a and b, respectively. Both Si/P2 and Si/SiO_x@C samples consist of aggregates of spherical particles with size in the range from tens to hundreds of nanometers. There is no noticeable difference between the morphology of Si/P2 and that of Si/SiO_x@C. Energy-dispersive X-ray spectroscopy (EDS) mapping of Si, O, and C elements in Si/SiO_x@C is shown in Fig. 1c, which verifies that these elements are uniformly distributed at the microscale. The contents of the elements derived from the EDS data were 48 wt% C, 27 wt% O, and 25 wt% Si. However, the EDS measurement is local and surface sensitive, and the data may not represent the real composition of the bulk. EDS cannot provide the contents of metallic Si or free carbon either. TEM images of Si/P2 and Si/SiO_x@C are shown in Fig. 1d–f. Crystalline Si particles embedded in an amorphous matrix are visible in all images. The TEM images show a fringe spacing of 0.31 nm, which matches the *d*-spacing of the (111) atomic layers of Si. The average particle size of the Si particles was estimated to be in the range of 20–50 nm.

In order to understand the chemical evolution during the synthesis process, we used FTIR spectroscopy to analyze P1, Si/P2 and Si/SiO_x@C, and the spectra are shown in Fig. 2a. The spectrum of P1 indicates the presence of Si–CH_3 groups at 779 (stretching) and 1261 cm^{-1} (bending) and Si–O–Si groups at 1015 cm^{-1} (asymmetric stretching).[29,44–46] At the same time, extensive Si-phenyl groups are identified by peaks at 695, 727, 1429 and 1593 cm^{-1}.[29,46] Surprisingly, we could not find any peaks of Si-phenyl groups in the spectrum of Si/P2 or Si/SiO_x@C. It looks like all phenyl groups were eliminated in Si/P2 after reduction. We could still detect strong peaks at 779 and 1261 cm^{-1} simultaneously in Si/P2, which indicates that there were still a large number of Si–CH_3 groups. The signal from the Si–CH_3 groups in Si/SiO_x@C was much weaker than that from Si/P2, suggesting that most methyl groups in P2 were carbonized during pyrolysis.

Fig. 2b shows the XRD patterns of Si/P2 and Si/SiO_x@C. Both patterns show typical reflections of crystalline Si. The sharp reflection around 28.5° and four other reflections at 47.4°, 56.2°, 69.3°, and 76.6° are from the (111), (220), (311), (400) and (331) lattice planes of cubic Si, respectively (JCPDS file card no. 65-1060),[47] confirming that Si from P1 was reduced to form elemental Si crystallites. Using the Scherrer equation, we estimated the average crystallite size of Si in Si/P2 to be 31 nm, which is consistent with the TEM observation. No other crystalline phases are identified in Si/P2. In the pattern of Si/SiO_x@C, we can also find a broad (002) peak of graphite at around 23°, indicating the presence of free carbon.[48] In order to obtain further information about C and Si, Raman spectra of Si/P2 and Si/SiO_x@C were collected. Fig. 2c confirms that crystalline Si is present in both samples, although there are subtle differences between the two spectra. The peaks are located at 503.9 cm^{-1} and 926.6 cm^{-1} in the spectrum of Si/P2, while they are at 497.4 cm^{-1} and 922.7 cm^{-1} in the spectrum of Si/SiO_x@C. The red-shift of the peak positions from the standard peak positions of bulk Si is due to the phonon confinement effect in nanostructures.[49] The presence of free carbon after pyrolysis can also be verified by Raman spectroscopy. The inset of Fig. 2c shows the enlarged spectrum of Si/SiO_x@C, in which we can identify the D and G bands at 1321.7 cm^{-1} and 1573.0 cm^{-1}, respectively. The ratio between the intensities I_D/I_G reflects the degree of disorder in the structure of carbon. In this case, I_D/I_G equals 1.148 which suggests that the carbon in the Si/SiO_x@C is relatively disordered.[30] The TEM, XRD, and Raman data all confirmed that Si was successfully reduced from the polysiloxane precursor. The bond cleavage between Si and O is likely to be caused by the attack of highly reductive solvated electrons produced in the ionization process ($Mg \rightarrow Mg^{2+} + 2e^-$) in a molten salt.[50] TGA of Si/SiO_x@C (Fig. 2d) shows a weight loss of 21 wt% upon heating in air to 800 °C, and the weight loss can be mainly attributed to the oxidation of free carbon.[51] Since the color of the Si/SiO_x@C sample changed from black to brownish after TGA (Fig. S1†), there should still be residual C atoms in the sample including those present in the Si–C bonds. Oxidation of metallic Si could have taken place as well during TGA, contributing to a weight gain of the sample. Since we did not have techniques to reliably measure the content of metallic Si and bonded Si in the bulk, it is difficult to derive the contents of Si, SiO_x, and C.

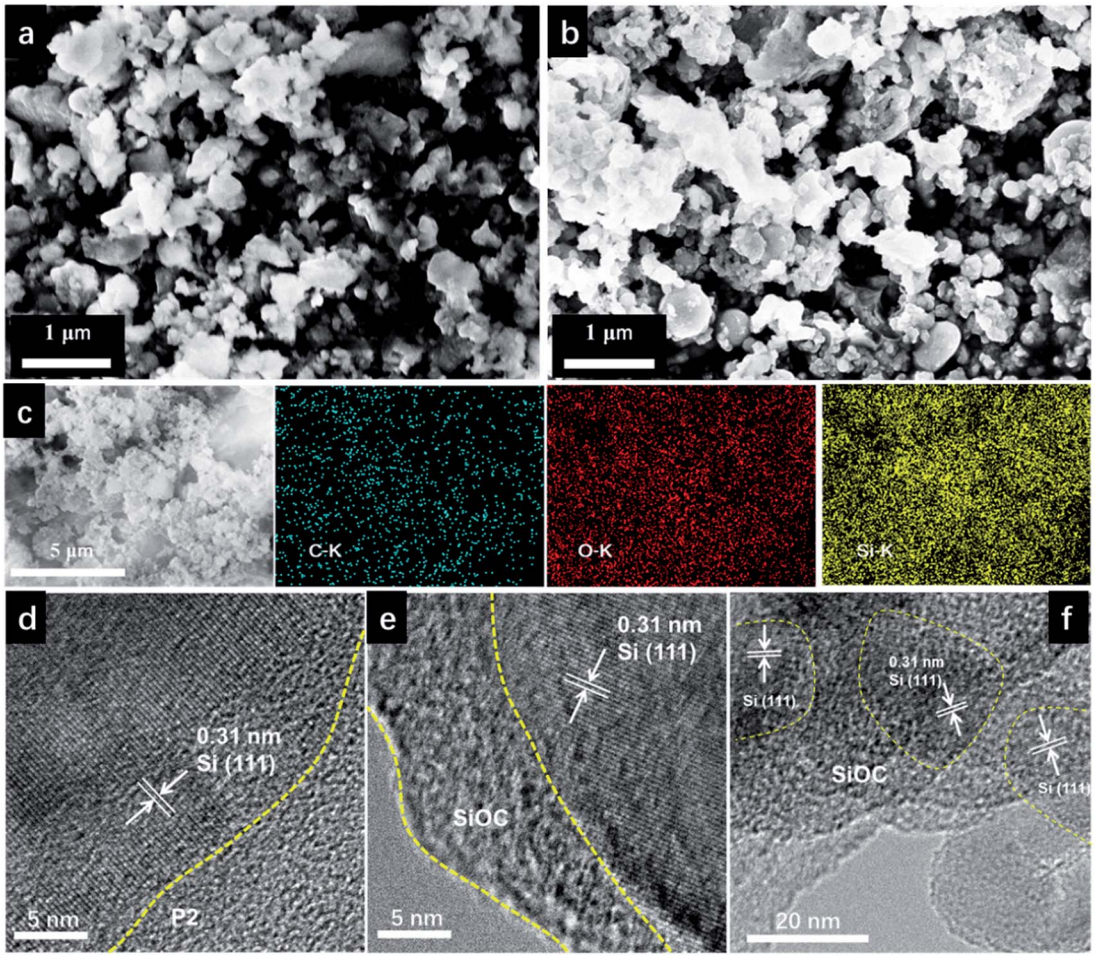

Fig. 1 SEM images of (a) Si/P2 and (b) Si/SiO_x@C; (c) EDS mappings of C, O, and Si in Si/SiO_x@C; TEM images of (d) Si/P2 and (e and f) Si/SiO_x@C.

XPS data further confirm the chemical states of the elements in Si/P2 and Si/SiO_x@C. Fig. S2† shows the survey spectrum of Si/SiO_x@C, in which one can detect peaks at around 103.08, 154.08, 284.08 and 533.08 eV, corresponding to Si 2p, Si 2s, C 1s, and O 1s, respectively. The adsorbed O, tape substrate, and Si–O bonds in the sample all contributed to the conspicuous O 1s peak at 533.08 eV.[52] The FTIR spectroscopy results indicate that the number of Si–C bonds decreased after pyrolysis, and the XPS spectra confirm this change. The Si 2p spectrum can be deconvoluted into three peaks, corresponding to the Si–Si bonds at around 99.2–99.5 eV, the Si–C bonds at around 101.5–101.9 eV, and the Si–O bonds at around 103.6–103.9 eV, respectively (Fig. 3a and b).[48,53] We can see that the relative content of the Si–C bonds diminished a lot after pyrolysis, suggesting the formation of free carbon. Similarly, the relative intensity of the C–Si bonds *vs.* the C–C bonds also decreased significantly after pyrolysis, as shown in the C 1s spectrum (Fig. 3c and d). Although the presence of Si–C bonds was observed in Si/SiO_x@C, there was no evidence of SiC crystals according to XRD. The Si–C bonds likely reside at the interface between the Si nanoparticles and the free carbon.

We evaluated the electrochemical performance of Si/SiO_x@C as an anode material for LIBs. The CV curves of LIBs with Si/SiO_x@C anodes at a scan rate of 0.2 mV s^{-1} are shown in Fig. 4a. The CV curve of the first cycle is apparently dissimilar from the following cycles. A broad cathodic peak appears in the first cycle and then vanishes, likely due to the initial electrolyte decomposition and the formation of a stable SEI film. The charging branch shows two oxidation peaks at 0.36 and 0.52 V, which could be ascribed to the lithium extraction process in Si. It is worth noting that the two oxidation peaks become stronger and stronger in subsequent cycles, which indicates that there might be an activation process in Si/SiO_x@C. The cathodic peak at 0.18 V becomes sharper and sharper during cycling, which suggests a gradual conversion from crystalline Si to amorphous Si.[48]

The performance of LIBs utilizing the Si/SiO_x@C anode was evaluated using galvanostatic charging/discharging measurements over the 0.01–2.0 V range. In order to evaluate the benefits of the Si/SiO_x@C anode, we also tested LIBs utilizing nano-crystalline Si (Fig. S3 and S4†) as the active material in the anode. Fig. 4b and c and S5† show the characteristic charging/discharging performance of Si/SiO_x@C, in comparison to nano-crystalline Si. As shown in Fig. S5,† in the first discharge curve, the sloping plateau from 1.5 V to 0.3 V can be related to the formation of a SEI layer and the reduction of SiO_x to Si,[30]

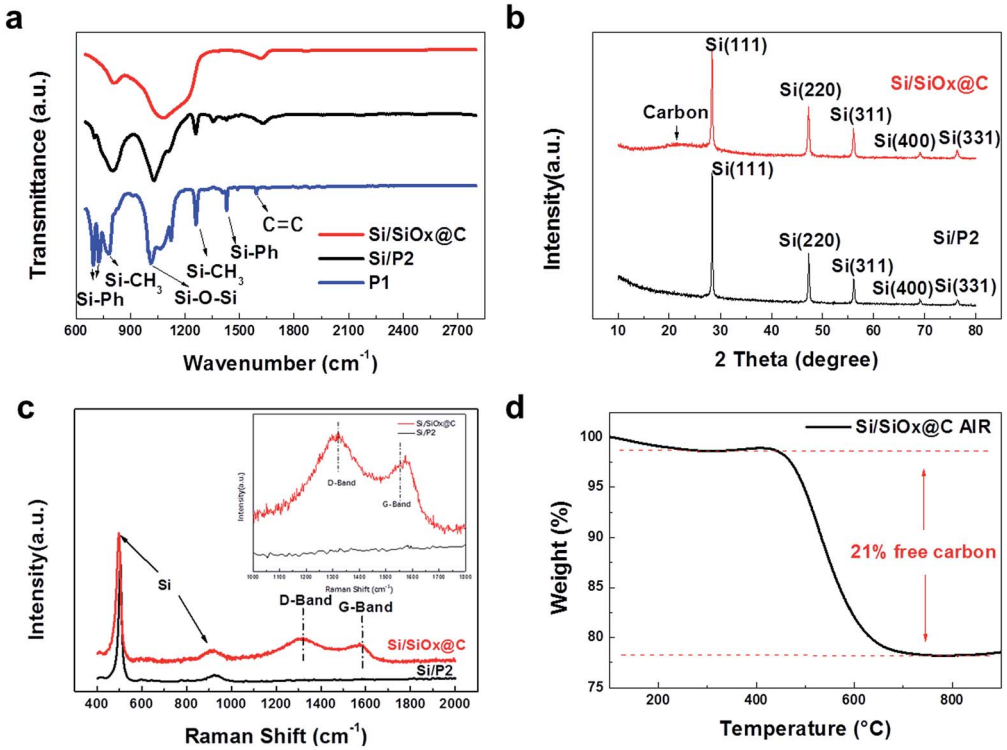

Fig. 2 (a) FTIR spectra of P1, Si/P2, and Si/SiO_x@C, (b) XRD patterns of Si/P2 and Si/SiO_x@C, (c) Raman spectra of Si/P2 and Si/SiO_x@C, (inset) enlarged region of 1000–1800 cm^{-1}, showing details of D and G bands of Si/SiO_x@C, and (d) TGA curve measured in air from 100 to 1000 °C at a heating rate of 10 °C min^{-1}, indicating that the free carbon content in the composite is about 21 wt%.

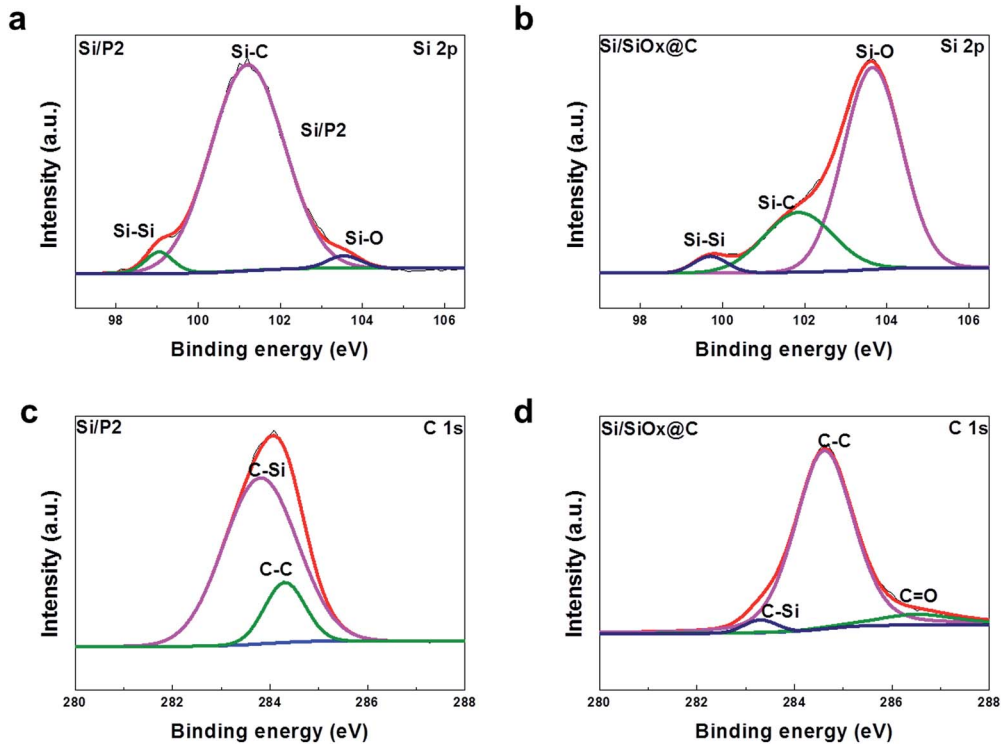

Fig. 3 High-resolution XPS spectra with Gaussian fitting of (a) Si 2p in Si/P2, (b) Si 2p in Si/SiO_x@C, (c) C 1s in Si/P2, and (d) C 1s in Si/SiO_x@C.

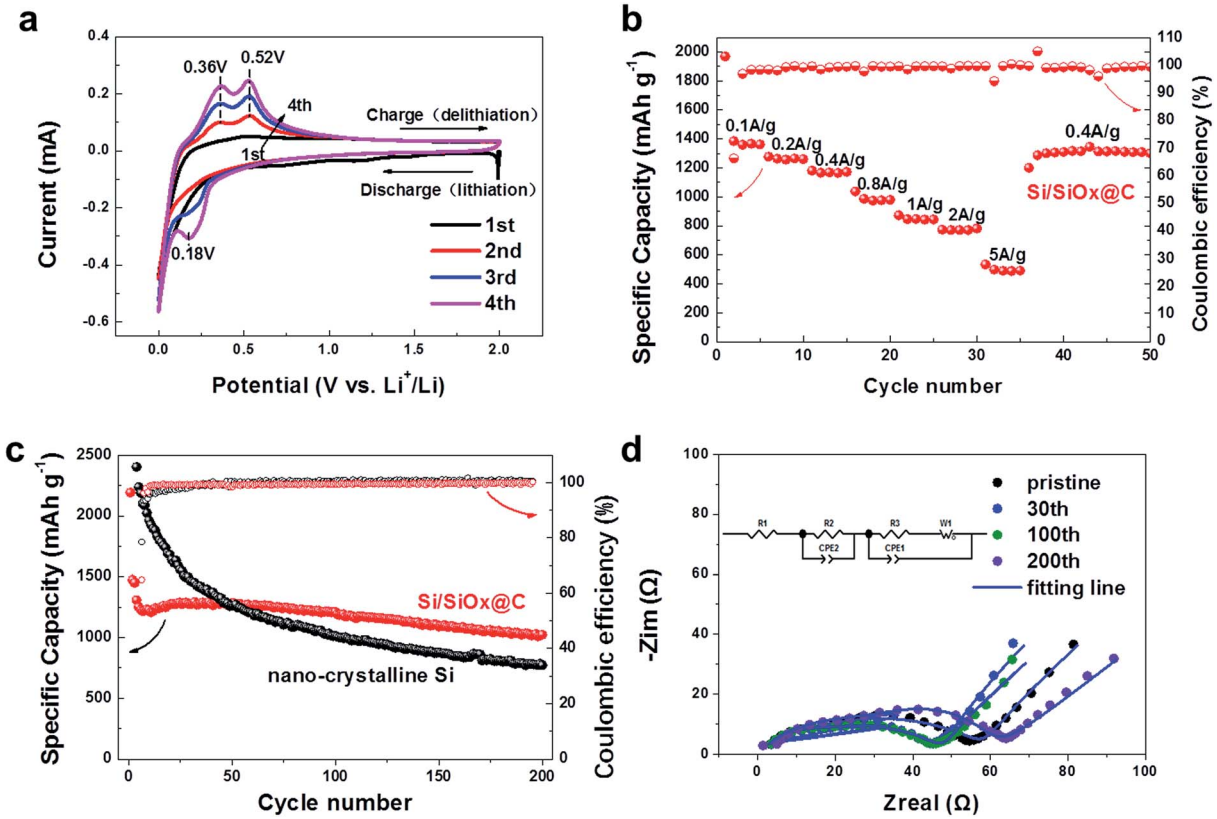

Fig. 4 Electrochemical measurement of the Si/SiO_x@C nanocomposite anode: (a) CV curves at a scan rate of 0.5 mV s^{-1}; (b) rate performance at various current densities. The voltage range is 0.01–2.0 V *vs.* Li^+/Li; (c) cycling performance and CE of Si/SiO_x@C compared to those of Si nanoparticles at a current density of 0.1 A g^{-1} for the 1st, 2nd and 3rd cycles, and then at 0.4 A g^{-1} for the latter cycles; (d) Nyquist plots of Si/SiO_x@C before cycling and after the 30th, 100th and 200th charging–discharging cycles, obtained after charging to 2.0 V.

resulting in the loss of capacity and a low initial coulombic efficiency of 63.6%. In subsequent cycles, the sloping plateau from 1.5 V to 0.3 V disappears, suggesting that the SEI layer is stable. The charging plateau from 0.3 V to 0.5 V can be ascribed to the lithium extraction, and it gradually extends starting from the 3rd cycle, suggesting that an activation process was likely taking place. In comparison, nano-crystalline Si showed a slightly higher initial coulombic efficiency (ICE) of 78.5% (Fig. S7†). The rate capability is an important indicator of the performance of Si-based anodes. The rate capability of the Si/SiO_x@C anode is presented in Fig. 4b at various current densities from 0.1 A g^{-1} to 0.2 A g^{-1}, 0.4 A g^{-1}, 1 A g^{-1}, 2 A g^{-1}, and 5 A g^{-1} and finally back to 0.4 A g^{-1}. Accordingly, the discharge capacity of Si/SiO_x@C changed from 1309.9 to 1214.7, 1118.6, 935.8, 797.8 and 448.2 mA h g^{-1} and finally came back to 1260.6 mA h g^{-1}. At 0.4 A g^{-1}, the final specific capacity was even higher than the original value, which is also an indicator of the gradual activation of Si secured by a stable nanocomposite structure.

Fig. 4c shows the cycling performance of nano-crystalline Si and Si/SiO_x@C anodes in the voltage range of 0.01–2.0 V at a constant current density of 0.4 A g^{-1}. At the beginning stage, the Si/SiO_x@C anode showed a slowly increasing capacity, indicating that the anode was gradually activated. The capacity of Si/SiO_x@C at the 200th cycle was 1023 mA h g^{-1}, corresponding to a capacity retention of 81.84% of the initial capacity. On the other hand, the nano-crystalline Si anode showed a very high initial capacity, but its capacity decayed sharply to 771 mA h g^{-1}, corresponding to a capacity retention of only 36.73%. To some extent, nano-crystalline Si is able to alleviate the fragmentation issue caused by volume change upon Li-ion insertion/extraction. However, we still observed significant capacity loss for nano-crystalline Si in LIBs. In contrast, SiO_x and the free carbon network provided mechanical support to buffer the strain caused by the volume change of Si in our Si/SiO_x@C nanocomposite. The SiO_x@C structure also isolates Si from being in direct contact with the electrolyte, and can effectively prevent continuous formation of the SEI. We also prepared a structurally similar Si@C composite by intercalating nano-crystalline Si into slightly exfoliated graphite (SEG) and filling the void space with amorphous carbon. A comparison between Si/SiO_x@C and Si@C in terms of cycling performance shows that the Si/SiO_x@C is superior (Fig. S8†). The cycling performance of Si/SiO_x@C is also comparable to those of other types of Si@C composite anode materials recently reported (Table S1†).

EIS (electrochemical impedance spectroscopy) measurements were conducted on LIBs with Si/SiO_x@C and nano-crystalline Si anodes at a current density of 0.4 A g^{-1} after ten cycles, with lithium ions fully extracted. In the Nyquist plots

shown in Fig. S9,† we can observe a depressed semicircle in the high/medium frequency range and a straight line in the low frequency range. The diameter of the depressed semicircle signifies the charge transfer resistance while the angled straight line is associated with the diffusion-controlled process. It can be seen that the Si/SiO_x@C demonstrated a smaller semicircle than nano-crystalline Si, indicating a smaller electrochemical reaction resistance in the Si/SiO_x@C composite electrode than the nano-crystalline Si. This implies that the Si/SiO_x@C anode has a higher electronic conductivity, which can be attributed to the continuous carbon network. The evolution of the electrochemical impedance of an LIB with the Si/SiO_x@C anode at different stages of cycling can be seen in Fig. 4d. There are two semicircles which likely originate from the charge transfer resistance at the Si/SiO_x@C interface and the SiO_x@C/electrolyte interface, and a sloping line representing the ion diffusion resistance, known as the Warburg impedance. From the 10^{th} cycle to the 100^{th} cycle, the resistance of the anode decreased due to activation, and finally stabilized at about 45 Ω. After 200 cycles, the resistance increased a little to about 63 Ω, suggesting that the Si/SiO_x@C anode can retain a high electronic conductivity through continuous cycling.

To reveal the structural change of the anode materials, the anodes were removed from the batteries after 200 charging/discharging cycles. There was no visible delamination in the Si/SiO_x@C anode, while delamination in the nano-crystalline Si anode was noticeable (Fig. S11†). Close examination of the anode surface by SEM reveals that there are many cracks in the nano-crystalline Si anode and Si nanoparticles are exposed, as shown in Fig. 5a. Apparently, the volume change of the anode layer during charging/discharging had caused cracking. Serious cracking can lead to detachment of the active material from the anode. Also, repeated cracking caused Si to be exposed to the electrolyte directly, leading to repeated damage and formation of a SEI. Therefore, the nano-crystalline Si anode showed marked capacity decay over 200 cycles. In contrast, cracks on the surface of the Si/SiO_x@C anode are much fewer and smaller, and the surface is safely covered by a mostly continuous SEI layer, as shown in Fig. 5b. For further analysis, the anodes were agitated in an ultrasonic bath to shake off the particles. Particles of Si and the binder from the nano-crystalline Si anode were easily separated and were well dispersed as shown in Fig. 5c. However, particles from the Si/SiO_x@C anode held up very well even after the ultrasound treatment, suggesting excellent mechanical strength. The TEM image of Si/SiO_x@C after the 200^{th} cycle can be found in Fig. S10.† Crystalline Si in the original Si/SiO_x@C anode changed to amorphous after repeated Li-ion insertion and extraction; however, the Si/SiO_x@C

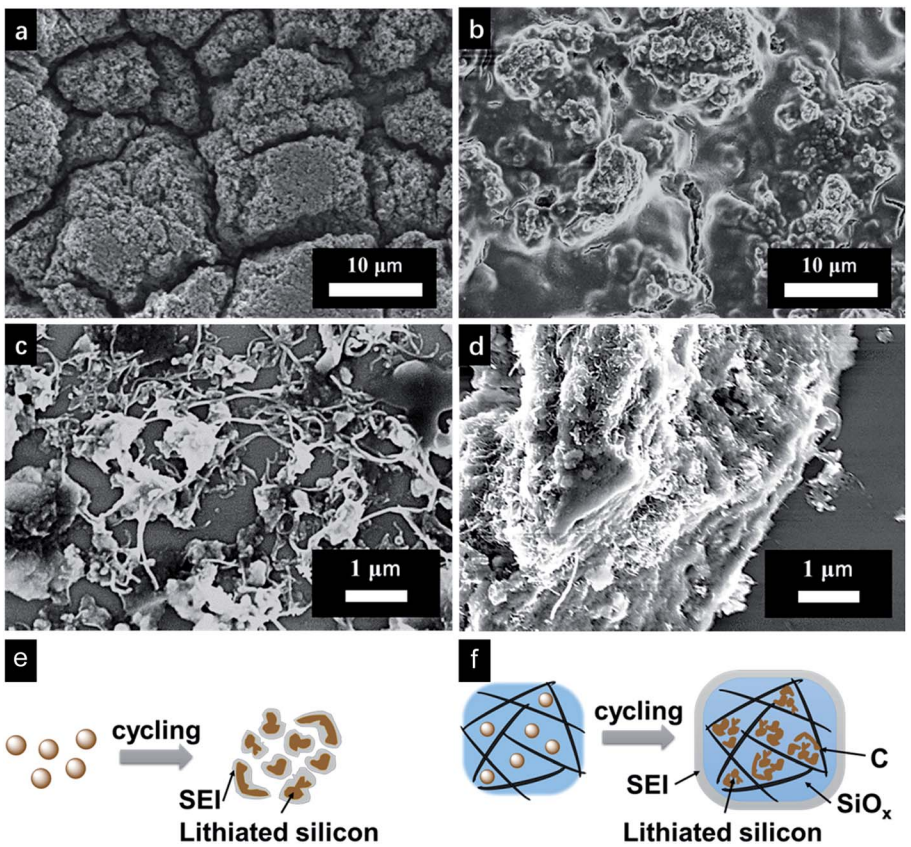

Fig. 5 SEM images of the electrode surface and removed particles after 200 cycles: (a) surface of the nano-crystalline Si electrode, (b) surface of the Si/SiO_x@C electrode, (c) particles from the nano-crystalline Si electrode, and (d) particles from the Si/SiO_x@C electrode. (e) Pulverization of nano-crystalline Si causes particle detachment and formation of a SEI between particles; (f) SiO_x@C matrix protects Si particles from detachment and forms a stable SEI enclosing the composite.

nanocomposite structure appears to be unaltered. The difference between the cycling behaviors of nano-crystalline Si and the Si/SiO_x@C nanocomposite has been schematically illustrated in Fig. 5e and f. For nano-crystalline Si, SEI films form around each individual particle and the volume change of the particles can easily cause the particles to separate from each other. If Si particles fracture due to volume change, the electrolyte will come into direct contact with the fresh fracture surface and a new SEI film will form, causing irreversible consumption of lithium. For the Si/SiO_x@C nanocomposite, Si nanoparticles are held in place by the SiO_x@C matrix and they are not in direct contact with the electrolyte, although electrons and lithium ions can transfer to the Si nanoparticles *via* the carbon network. SEI films only form on the outer surface of the Si/SiO_x@C nanocomposite particles. Even if the Si nanoparticles fracture, they are still inside the SiO_x@C matrix and the fracture surface will not be in contact with the electrolyte. Normally the Si/SiO_x@C nanocomposite will not break easily because the matrix itself is not supposed to change volume during lithium transfer. Therefore the SEI on the outer surface of the nanocomposite can be maintained and there will be no unnecessary lithium consumption due to new SEI formation.

Conclusions

In conclusion, we used a novel and simple method to prepare an *in situ* Si/SiO_x@C nanocomposite, which demonstrated great potential as an anode material for lithium-ion batteries. Polysiloxane was used as the only single precursor to generate both the Si for lithium storage and the SiO_x@C matrix for buffering the volume change as well as providing a highly conductive network for electrons and ions. The as-synthesized nanocomposite showed superior rate performance and cycling stability, in comparison to nano-crystalline Si. Potentially, the performance of the Si/SiO_x@C nanocomposite anode can be further optimized by tuning the Si/C ratio *via* facile chemical synthesis of various polysiloxane precursors. It is worth mentioning that the method can be scaled up, which allows the Si/SiO_x@C to become a potential candidate for next generation anode materials for LIBs.

Acknowledgements

This research was financially supported by the National Materials Genome Project (2016YFB0700600), the Guangdong Innovation Team Project (No. 2013N080), and the Shenzhen Science and Technology Research Grants (No. JCYJ20150626110958181 and JCYJ20150518092933435).

Notes and references

1 B. H. Chen, S. I. Chuang, W. R. Liu and J. G. Duh, *ACS Appl. Mater. Interfaces*, 2015, **7**, 28166–28176.
2 Y. Kubota, M. C. S. Escaño, H. Nakanishi and H. Kasai, *J. Appl. Phys.*, 2007, **102**, 053704.
3 M. Gu, X. C. Xiao, G. Liu, S. Thevuthasan, D. R. Baer, J. G. Zhang, J. Liu, N. D. Browning and C. M. Wang, *Sci. Rep.*, 2014, **4**, 3684.
4 Y.-Y. Huang, D. Han, Y.-B. He, Q. Yun, M. Liu, X. Qin, B. Li and F. Kang, *Electrochim. Acta*, 2015, **184**, 364–370.
5 L.-F. Cui, Y. Yang, C.-M. Hsu and Y. Cui, *Nano Lett.*, 2009, **9**, 3370–3374.
6 C. K. Chan, H. Peng, G. Liu, K. McIlwrath, X. F. Zhang, R. A. Huggins and Y. Cui, *Nat. Nanotechnol.*, 2007, **3**, 31–35.
7 L. Hu, H. Wu, S. S. Hong, L. Cui, J. R. McDonough, S. Bohy and Y. Cui, *Chem. Commun.*, 2011, **47**, 367–369.
8 M.-H. Park, M. G. Kim, J. Joo, K. Kim, J. Kim, S. Ahn, Y. Cui and J. Cho, *Nano Lett.*, 2009, **9**, 3844–3847.
9 H. Wu, G. Chan, J. W. Choi, I. Ryu, Y. Yao, M. T. McDowell, S. W. Lee, A. Jackson, Y. Yang, L. Hu and Y. Cui, *Nat. Nanotechnol.*, 2012, **7**, 310–315.
10 N. Liu, K. Huo, M. T. McDowell, J. Zhao and Y. Cui, *Sci. Rep.*, 2013, **3**, 1919.
11 B. Zhu, Y. Jin, Y. Tan, L. Zong, Y. Hu, L. Chen, Y. Chen, Q. Zhang and J. Zhu, *Nano Lett.*, 2015, **15**, 5750–5754.
12 N. Lin, Y. Han, J. Zhou, K. Zhang, T. Xu, Y. Zhu and Y. Qian, *Energy Environ. Sci.*, 2015, **8**, 3187–3191.
13 Y. Yao, M. T. McDowell, I. Ryu, H. Wu, N. Liu, L. Hu, W. D. Nix and Y. Cui, *Nano Lett.*, 2011, **11**, 2949–2954.
14 Z. Lu, N. Liu, H.-W. Lee, J. Zhao, W. Li, Y. Li and Y. Cui, *ACS Nano*, 2015, **9**, 2540–2547.
15 H. Zhong, H. Zhan and Y.-H. Zhou, *J. Power Sources*, 2014, **262**, 10–14.
16 Y. Hwa, W.-S. Kim, B.-C. Yu, S.-H. Hong and H.-J. Sohn, *Energy Technol.*, 2013, **1**, 327–331.
17 Y. Jiang, H. Wang, B. Li, Y. Zhang, C. Xie, J. Zhang, G. Chen and C. Niu, *Carbon*, 2016, **107**, 600–606.
18 N. Kobayashi, Y. Inden and M. Endo, *J. Power Sources*, 2016, **326**, 235–241.
19 M. Ko, S. Chae, J. Ma, N. Kim, H.-W. Lee, Y. Cui and J. Cho, *Nat. Energy*, 2016, **1**, 16113.
20 H. Wu, G. Yu, L. Pan, N. Liu, M. T. McDowell, Z. Bao and Y. Cui, *Nat. Commun.*, 2013, **4**, 1943.
21 D. Lin, W. Liu, Y. Liu, H. R. Lee, P.-C. Hsu, K. Liu and Y. Cui, *Nano Lett.*, 2016, **16**, 459–465.
22 Y. Sun, J. Lopez, H.-W. Lee, N. Liu, G. Zheng, C.-L. Wu, J. Sun, W. Liu, J. W. Chung, Z. Bao and Y. Cui, *Adv. Mater.*, 2016, **28**, 2455–2461.
23 N. Liu, H. Wu, M. T. McDowell, Y. Yao, C. Wang and Y. Cui, *Nano Lett.*, 2012, **12**, 3315–3321.
24 C. Wang, H. Wu, Z. Chen, M. T. McDowell, Y. Cui and Z. Bao, *Nat. Chem.*, 2013, **5**, 1042–1048.
25 Z. Chen, C. Wang, J. Lopez, Z. Lu, Y. Cui and Z. Bao, *Adv. Energy Mater.*, 2015, **5**, 1401826.
26 N. Liu, Z. Lu, J. Zhao, M. T. McDowell, H.-W. Lee, W. Zhao and Y. Cui, *Nat. Nanotechnol.*, 2014, **9**, 187–192.
27 Y. Yao, N. Liu, M. T. McDowell, M. Pasta and Y. Cui, *Energy Environ. Sci.*, 2012, **5**, 7927.
28 Y. Li, K. Yan, H.-W. Lee, Z. Lu, N. Liu and Y. Cui, *Nat. Energy*, 2016, **1**, 15029.
29 M. Halim, C. Hudaya, A. Y. Kim and J. K. Lee, *J. Mater. Chem. A*, 2016, **4**, 2651–2656.

30 M. Ma, H. Wang, M. Niu, L. Su, X. Fan, J. Deng, Y. Zhang and X. Du, *RSC Adv.*, 2016, **6**, 43316–43321.
31 V. S. Pradeep, D. G. Ayana, M. Graczyk-Zajac, G. D. Soraru and R. Riedel, *Electrochim. Acta*, 2015, **157**, 41–45.
32 A. Guo, M. Roso, P. Colombo, J. Liu and M. Modesti, *J. Mater. Sci.*, 2015, **50**, 2735–2746.
33 X. Liu, K. Xie, J. Wang, C. Zheng and Y. Pan, *J. Mater. Chem.*, 2012, **22**, 19621.
34 Y. Chen, S. Zeng and X. Ai, *Chin. Sci. Bull.*, 2013, **31**, 3233.
35 J. Cui, Y. Cui, S. Li, H. Sun, Z. Wen and J. Sun, *ACS Appl. Mater. Interfaces*, 2016, **8**, 30239–30247.
36 F. Dai, R. Yi, M. L. Gordin, S. Chen and D. Wang, *RSC Adv.*, 2012, **2**, 12710.
37 H. Jung, B. C. Yeo, K. R. Lee and S. S. Han, *Phys. Chem. Chem. Phys.*, 2016, **18**, 32078–32086.
38 Y. Ren and M. Li, *J. Power Sources*, 2016, **306**, 459–466.
39 J. Kaspar, M. Graczyk-Zajac, S. Lauterbach, H.-J. Kleebe and R. Riedel, *J. Power Sources*, 2014, **269**, 164–172.
40 D. Vrankovic, K. Wissel, M. Graczyk-Zajac and R. Riedel, *Solid State Ionics*, 2017, **302**, 66–71.
41 K. H. Kim, D. J. Lee, K. M. Cho, S. J. Kim, J.-K. Park and H.-T. Jung, *Sci. Rep.*, 2015, **5**, 9014.
42 J. Wang, M. Zhou, G. Tan, S. Chen, F. Wu, J. Lu and K. Amine, *Nanoscale*, 2015, **7**, 8023–8034.
43 J. Wang, W. Bao, L. Ma, G. Tan, Y. Su, S. Chen, F. Wu, J. Lu and K. Amine, *ChemSusChem*, 2015, **8**, 4073–4080.
44 Y. S. Kim, Y. L. Joo and Y.-J. Kwark, *J. Mater. Sci. Technol.*, 2016, **32**, 195–199.
45 T. Takahashi, H. Munstedt, P. Colombo and M. Modesti, *J. Mater. Sci.*, 2001, **36**, 1627–1639.
46 Z. Yang, L. Feng, S. Diao, S. Feng and C. Zhang, *Thermochim. Acta*, 2011, **521**, 170–175.
47 Y.-C. Zhang, Y. You, S. Xin, Y.-X. Yin, J. Zhang, P. Wang, X.-s. Zheng, F.-F. Cao and Y.-G. Guo, *Nano Energy*, 2016, **25**, 120–127.
48 W. Ren, Y. Wang, Z. Zhang, Q. Tan, Z. Zhong and F. Su, *J. Mater. Chem. A*, 2016, **4**, 552–560.
49 H. Xia, Y. L. He, L. C. Wang, W. Zhang, X. N. Liu, X. K. Zhang, D. Feng and H. E. Jackson, *J. Appl. Phys.*, 1995, **78**, 6705–6708.
50 X. Liu, C. Giordano and M. Antonietti, *J. Mater. Chem.*, 2012, **22**, 5454.
51 S. Choi, D. S. Jung and J. W. Choi, *Nano Lett.*, 2014, **14**, 7120–7125.
52 Z. Wen, G. Lu, S. Cui, H. Kim, S. Ci, J. Jiang, P. T. Hurley and J. Chen, *Nanoscale*, 2014, **6**, 342–351.
53 Z. Sun, X. Wang, T. Cai, Z. Meng and W.-Q. Han, *RSC Adv.*, 2016, **6**, 40799–40805.